Engineering defects in TiO$_2$ for the simultaneous production of hydrogen and organic products

Jiajun Zhang [a], Cui Ying Toe [a,b,*], Priyank Kumar [a], Jason Scott [a,**], Rose Amal [a]

[a] School of Chemical Engineering, The University of New South Wales, Sydney, New South Wales 2052, Australia
[b] School of Engineering, University of Newcastle, Callaghan, New South Wales 2308, Australia

ARTICLE INFO

ABSTRACT

Photoreforming ethanol to simultaneously produce hydrogen and value-added organic products was realized over defected TiO$_2$. Chemically induced defects in TiO$_2$ promoted light absorption and charge separation, enhancing overall photoactivity. The induced defects also regulated product selectivity, leading to greater hydrogen purity and liquid to gaseous carbon ratio. The optimal catalyst generated 0.08 mmol/hr of hydrogen with a purity greater than 99 % and 0.08 mmol/hr of liquid acetaldehyde over a 6 hr timeframe. This was three times greater than the untreated TiO$_2$. Active species trapping revealed that the preferred ethanol oxidation pathway was direct hole transfer, indicating the selectivity relies on surface chemisorption. Surface defects decreased the acetaldehyde adsorption energy, instigating its prompt desorption and suppressing overoxidation into CO$_2$, thus improving the selectivity towards hydrogen and liquid hydrocarbon products. The work offers an alternative approach towards sustainable energy by coupling photocatalysis with waste organic utilization.

1. Introduction

Hydrogen (H$_2$) is viewed as a sustainable energy carrier due to its emission free nature and earth abundancy [1,2]. Generating H$_2$ using renewable energy sources, in particular solar energy, could further ensure its feasibility for practical application [3]. As a process that enables direct conversion of solar to chemical energy, photocatalytic water splitting has attracted extensive attention within the research community. However, water splitting is an uphill reaction that requires a net energy input which creates an obvious thermodynamic obstacle [4,5]. Product separation is also a challenge for photocatalytic water splitting as H$_2$ and O$_2$ are generated as a mixture in the gas phase, causing safety concerns [6]. As an alternative, an organic substrate can be added to the system to boost the oxidation reaction and improve the overall rate of photocatalytic H$_2$ evolution. The slow water oxidation reaction, which is often the rate determining step during water splitting, is then substituted by a more rapid organic oxidation reaction [7,8]. Further, oxygen evolution can be avoided under appropriate operating conditions, in preference to partial oxidation of the organic substrate.

Using biomass as the organic substrate for photocatalytic H$_2$ generation (also known as photoreforming) has attracted significant attention

due to a high abundancy, sustainability and the carbon emission neutrality of biomass. However, in many cases, chemical structure complexity of the biomass (e.g., glycerol, 5-hydroxymethylfurfural, lignin) is a barrier to its application [9–11]. Ethanol is a simple organic compound that has been widely used to improve photocatalytic H$_2$ evolution performance [12,13]. Photoreforming requires only a low ethanol concentration (i.e. 5–10 v/v %) to achieve enhanced photocatalytic performance, opening the door to using low-concentration bioethanol which is readily produced from fermentation broth [14, 15]. Due to the hygroscopic nature of ethanol, the purification of fermentation broth (often containing ~10 % ethanol) into absolute ethanol is an energy intensive process [16]. Consequently, using low concentration ethanol as a photoreforming feedstock offers a more accessible and economical application of bioethanol.

Prior studies mostly employed ethanol solely as a hole scavenger and did not consider the oxidation reaction pathway [17,18]. The focus of these works was typically devoted to H$_2$ evolution rather than the photo-oxidation reaction. Nevertheless, controlling the organic oxidation selectivity is highly desirable as it provides an opportunity for the generation of value-added organic products alongside the H$_2$. The simultaneous production of gas-phase H$_2$ and valuable liquid-phase

---

organic products means post reaction separation and purification processes can also be simplified, improving the economics of the photoreforming reaction. To establish a selective photoreforming system, a detailed investigation of the photooxidation reaction pathways is needed. The possible by-products from ethanol photoreforming include CO, CH_4, CO_2 in the gas phase, and acetaldehyde, acetic acid, 1,1-diethoxyethane, 2,3-butane-diol in the liquid phase [18–20]. While some studies demonstrated the potential formation of gas phase carbon-based products, liquid phase products were rarely identified and quantified [18]. Ideally, the ethanol photoreforming process should cease upon the formation of valuable products (such as acetaldehyde or acetic acid), to prevent further oxidation to carbon containing gases.

Introducing defects into a semiconductor, such as TiO_2, has been shown to improve its performance as a photocatalyst. Chen et al. reported that high pressure H_2 calcination yielded "black TiO_2" with improved photocatalytic H_2 evolution performance [21]. The enhanced performance was attributed to the oxygen vacancies (O_v) that create a sub-band within the band structure for better light absorption as well as suppressed charge carrier recombination. O_v on TiO_2 have also been reported to regulate the photodegradation reaction pathway by tuning the surface properties. On introducing surface defects and terminal -OH groups on TiO, OH• formation was suppressed while H_2O_2 and•O_2^- generation were encouraged, altering the reactive species involved in the reaction [22]. In the case of gold-loaded defected TiO_2, highly selective photoreforming was achieved for pure ethanol as the reactant. In-situ FTIR demonstrated that the O_v influenced surface adsorption of the reactant and regulated the selectivity towards H_2 [23]. Given the suppression of highly oxidizing OH• radicals and preferential adsorption of reactant or intermediate products are considered to be key approaches to deliver high selectivity, defect engineering represents a promising approach to achieve selective photoreforming [24].

Herein, we report on the selective photoreforming of a 10 v/v % ethanol aqueous solution using defect-engineered TiO_2 for simultaneous production of H_2 gas and acetaldehyde. While defect engineering has often been employed to improve photocatalytic H_2 generation and ethanol photoreforming, its impact on the ethanol oxidation reaction pathway in aqueous solution is not understood. While Zhang et al. demonstrated the use of Au-loaded defected TiO_2 for enhanced activity and selectivity during pure ethanol photoreforming, our work is distinct in that it examines the key role the O_v on pristine TiO_2 in enhancing selectivity during ethanol photoreforming [23]. In this way, any simultaneous enhancement provided by the Au co-catalyst to the reaction is removed in the work. In addition, the 10 v/v % aqueous ethanol solution used here is a practical concentration in terms of potential future application. Finally, a detailed reaction pathway has been experimentally revealed in this work via intermediate radical trapping experiments.

2. Experimental

2.1. Chemicals

All chemicals were used as received without further purification. P25 TiO_2 was purchased from Aeroxide. Sodium borohydride ($NaBH_4$), dimethylsulfoxide (DMSO), coumarin, 5,5-dimethyl-1-pyrroline N-oxide (DMPO) and potassium permanganate ($KMnO_{4)}$ were purchased from Sigma-Aldrich. Absolute ethanol was provided by Chem-Supply, Australia.

2.2. Defect generation

A simple chemical reduction process was used to introduce defects into bare TiO_2 as reported with modification [25,26]. Typically, 1 g of P25 TiO_2 and a certain amount of $NaBH_4$ (0.2–0.7 g) were mixed by grinding. The mixture was transferred to a ceramic boat and heated in an Ar environment at a ramp rate of 5 °C/min to 350 °C where it was held

for 30 min. Following heat treatment, the solid product was washed with Mill-Q water three times and then dried under vacuum at 40 °C overnight before grinding. The defected TiO_2 catalysts are named according to the amount of $NaBH_4$ used with respect to TiO_2 (denoted as X), RT-X. P25 was also calcined under the same condition without addition of $NaBH_4$ and was used as bare TiO_2 sample.

2.3. Physical characterization

Transmission electron microscopy images were measured on a Philips CM200 Transmission electron microscope. X-ray diffraction patterns (XRD) were collected by a Xpert Multipurpose X-ray Diffraction System with Cu Kα radiation (λ = 0.15406 nm) at 45 kV and 40 mA with a scanning rate of 5° /min from 20° to 80°. UV–vis spectra of solid samples were collected from a Shimadzu UV-3600 UV–visible spectrophotometer with $BaSO_4$ as reference. The specific surface areas were calculated by the Brunauer-Emmett-Teller (BET) method. N_2 adsorption-desorption isotherms, surface areas, and pore parameters of the samples were determined at − 196 °C on a Micrometric Tristar 3030 adsorption analyser. The samples were degassed at 150 °C under vacuum for 3 hrs prior to analysis. Raman spectra were taken on a Renishaw inVia2 Raman Microscope with 532 nm laser. X-ray photoelectron spectroscopy (XPS) analyses were conducted on a Thermo Scientific ESCALAB250Xi X-Ray photoelectron spectrometer and calibrated using the C 1s peak of adventitious carbon to 284.8 eV. Photoluminescence spectra (PL) were collected on a Renishaw inVia Qontor Raman spectrometer with a 325 nm laser as the light source. Electron paramagnetic resonance (EPR) spectra were recorded on a Bruker EMX X-Band ESR Spectrometer at 120 K and room temperature (293 K). Photoelectrodes employed for photoelectrochemical (PEC) studies were prepared via drop-casting method. Typically, 2.5 mg of the catalyst was dispersed in 2 ml ethanol by sonication. The suspension was then drop-cast on a FTO glass slide with casting area of 1 cm^2. For PEC measurements, 0.2 M Na_2SO_4 solution was used as the electrolyte with Pt wire as the counter electrode, Ag/AgCl electrode as the reference electrode and the drop-cast TiO_2 photoelectrode as the working electrode. A 300 W Xe lamp with a 420 nm cut off filter was employed as the light source. A Metrohm PGSTAT302N Autolab electrochemical workstation was used to conduct the PEC studies in this work.

2.4. Photoreaction setup

A glass spiral reactor was used to test the photocatalytic performance of the prepared TiO_2 catalysts. In a typical photoreaction, 50 mg of catalyst was dispersed in 100 ml of 10 v/v % ethanol solution via sonication. The reaction suspension was then transferred to the spiral reactor system containing gas and liquid circulation pumps, a gas-liquid separator and a glass spiral reactor surrounding a UV fluorescence lamp (20 W, 4.7 mW/cm^2) positioned in an enclosed box (Scheme S1a). The spiral reactor was connected to a six-port valve and a GC (GC 2014, Shimazu equipped with a Thermal Conductivity Detector (TCD) and a Flame Ionization Detector (FID - with attached methanizer) for automated gas sampling and analysis. The known detection limit of H_2 on the TCD is 2×10^{-4} mmol/L. The known detection limit of CO, CO_2 and CH_4 on the FID is 4.2×10^{-6} mmol/L. Liquid samples were collected after the photoreaction. The collected liquid samples were filtered, sealed, and stored in a refrigerator to minimize the evaporation of volatile organic reactants and products (e.g., ethanol and acetaldehyde). A Bruker Avance III 600 MHz Nuclear Magnetic Resonance (NMR) Spectrometer was used to identify and quantify the organics in the liquid product at a 10^{-6} mmol/L detection limit. Sodium acetate in D_2O solution was used as the external standard for quantification. The identification of liquid product was shown in Fig. S1 and Table. S1.

2.5. Stability test on activity and selectivity

To exam the stability of catalysts in real reaction, a 24 h continuous reaction was conducted with 20 mg RT-0.5. For the selectivity aspect, RT-0.5 was tested to ensure its stability. In this test, 80 mg catalysts and 100 ml 10 v/v % ethanol solution were used for 6 h as the first cycle. Following the reaction, liquid sample was collected, and the products were quantified. The catalyst particles were collected on a filter membrane and dispersed in a new batch of 100 ml 10 v/v % ethanol solution. The stability test involved four repeat cycles, and the H_2 purity and liquid to gas phase carbon selectivity were calculated.

2.6. Active species (OH• and H_2O_2) trapping experiments

P25 TiO_2, RT-0.5 and RT-0.7 were selected to conduct active species (OH• and H_2O_2) trapping experiments. The detection of OH• was performed using two different probe molecules: DMSO and coumarin. A similar reaction setup and experimental conditions were used as described for the photoreaction where the 10 v/v % ethanol solution was replaced with 1 mM DMSO or 1 mM coumarin in 10 v/v % ethanol solution. For the DMSO test, the amount of recovered DMSO was quantified by NMR, while for the coumarin test, the formation of 7-hydroxycoumarin species (generated when coumarin reacts with OH• radicals) was detected by a fluorescence spectrophotometer (Horiba Fluoromax-4) at 456 nm with 350 nm laser excitation. The detection of H_2O_2 was achieved using the $KMnO_4$ method. Again, a similar reaction setup and experimental conditions were used as described for the photoreaction where the 10 v/v % ethanol solution was replaced with Mill-Q water. To minimize exposure to air, a syringe filled with certain amount of 1 mM $KMnO_4$ solution was used to take a liquid sample from the reaction bottle while the UV lamp was on. A reference solution was prepared and with light absorption at 525 nm being the basis for comparison. Further experimental details are provided in Note. S1 and Fig. S2 in Supporting Information.

2.7. Intermediate radical trapping experiment

10 ml 10 v/v % ethanol solution, 20 µl DMPO and 10 mg RT-0.5 was mixed and purged with N_2. UV irradiation was applied for 0.5 h. The collected liquid sample was filtered and tested with EPR.

2.8. Density functional theory (DFT) calculation

The VASP code was used for all DFT calculations. The core electrons were treated using the projector augmented wave method (PAW) method, and the Perdew-Burke-Ernzerhof (PBE) exchange-correlation functional was employed. A kinetic energy cut-off value of 500 eV was used for wavefunctions and a gamma-point k-grid was used for surface slab calculations. All relaxations proceeded until the residual forces on atoms were less than 0.03 eV/Å. A vacuum region greater than 10 Å in the direction normal to the sheets was used to avoid interactions between periodic images. The GGA+U method was then employed on the relaxed structure, with a U value of 6 eV, to correctly describe the TiO_2 band structure. A TiO_2 surface slab model (9.962 Å x 11.504 Å) was used, which contained an O-terminated TiO_2 (110) surface (containing 36 Ti atoms and 74 O atoms).

3. Results and discussion

3.1. Basic characterization

HRTEM images of bare and defected TiO_2 are provided in Fig. 1. As shown in Fig. 1a, the lattice spacing of bare P25 TiO_2 is ~0.35 nm, which is assigned to the (101) plane of the TiO_2 anatase phase (JCPDS No. 21-1272). Similarly, rutile phase (JCPDS No. 21-1276) with a lattice spacing of ~0.324 nm, assigned to the (110) plane, is observed. While a clear crystal lattice is displayed in the bulk of the bare TiO_2, RT-0.5 exhibits an approximately 1–2 nm disordered outer layer with crystalline core (lattice spacings of 0.35 nm and 0.324 nm) on both anatase and rutile phases, as illustrated in Fig. 1b and c [27,28].

The bulk crystal structure was characterized by XRD. As shown in Fig. S3a, all samples contain anatase (A) (JCPDS no. 21-1272) and rutile (R) (JCPDS no. 21-1276) phases corresponding to P25 that has an anatase: rutile ratio of 3:1 [21]. The diffraction peaks located at 25.3°, 27.5°, 36.0°, 37.8°, 41.2°, 55.1°, 62.7°, and 75.0° were assigned to crystal planes A(101), R(110), R(101), A(004), R(111), A(200), A(211), A(204), A(220) and A(215), respectively. The XRD patterns of all the samples are similar (no significant peak shifting or broadening), indicating that the crystallinity and crystal phases were not altered by the chemical reduction process. It has been reported that disorder in a crystal structure may cause diffraction peak shifting [29,30]. However, due to the low defect concentration on the defected samples (predominantly at the surface), there is no obvious peak shift in the XRD patterns. N_2 adsorption-desorption isotherms and BET specific surface areas of P25 and RT-0.5 are shown in Fig. S3b and Table S2. P25 and RT-0.5 have similar isotherms, BET specific surface areas (~66 $m^2 g^{-1}$) and BJH pore distributions, indicating little change to the physical structure of the particles during the chemical reduction process.

To further investigate the observed crystal lattice disorder, Raman studies were conducted on bare and defected TiO_2. As shown in the Raman spectra (Fig. S4), six different modes including 3Eg (144, 196, 639 cm^{-1}), 2B1g (397 and 519 cm^{-1}) and 1A1g (513 cm^{-1}) are observed, indicating the presence of tetragonal anatase as the dominant species [31,32]. The observation is in agreement with the XRD results that were indexed to a dominant anatase phase (Fig. S3a). Further analysis of the Raman spectra demonstrates that there is a broadening of the Eg peak at ~ 144 cm^{-1} for all the defected TiO_2 samples when compared to bare TiO_2. Raman spectra for all samples in the region of 100–250 cm^{-1} are shown in Fig. 2a with the full width at half maximum of Eg (1) listed in Table S3. The peak broadening highlights the distortion of the crystal structure upon high temperature chemical reduction. The thermal degradation of $NaBH_4$ at high temperature released H_2,
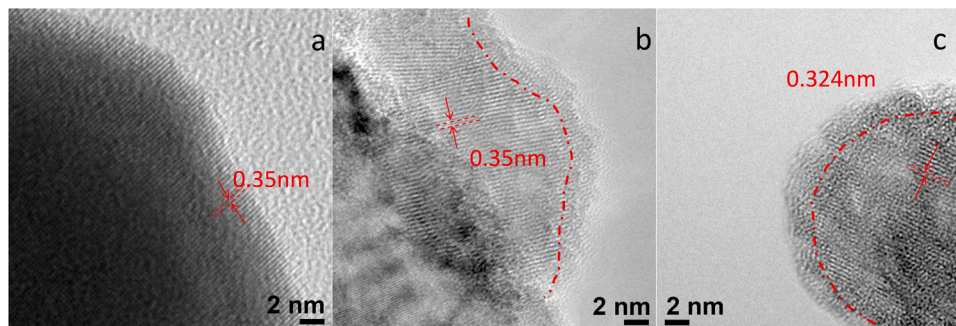

Fig. 1. HRTEM images of (a) bare P25, (b) RT-0.5(anatase) and (c) RT-0.5(rutile). The dotted line indicates the disordered layer.
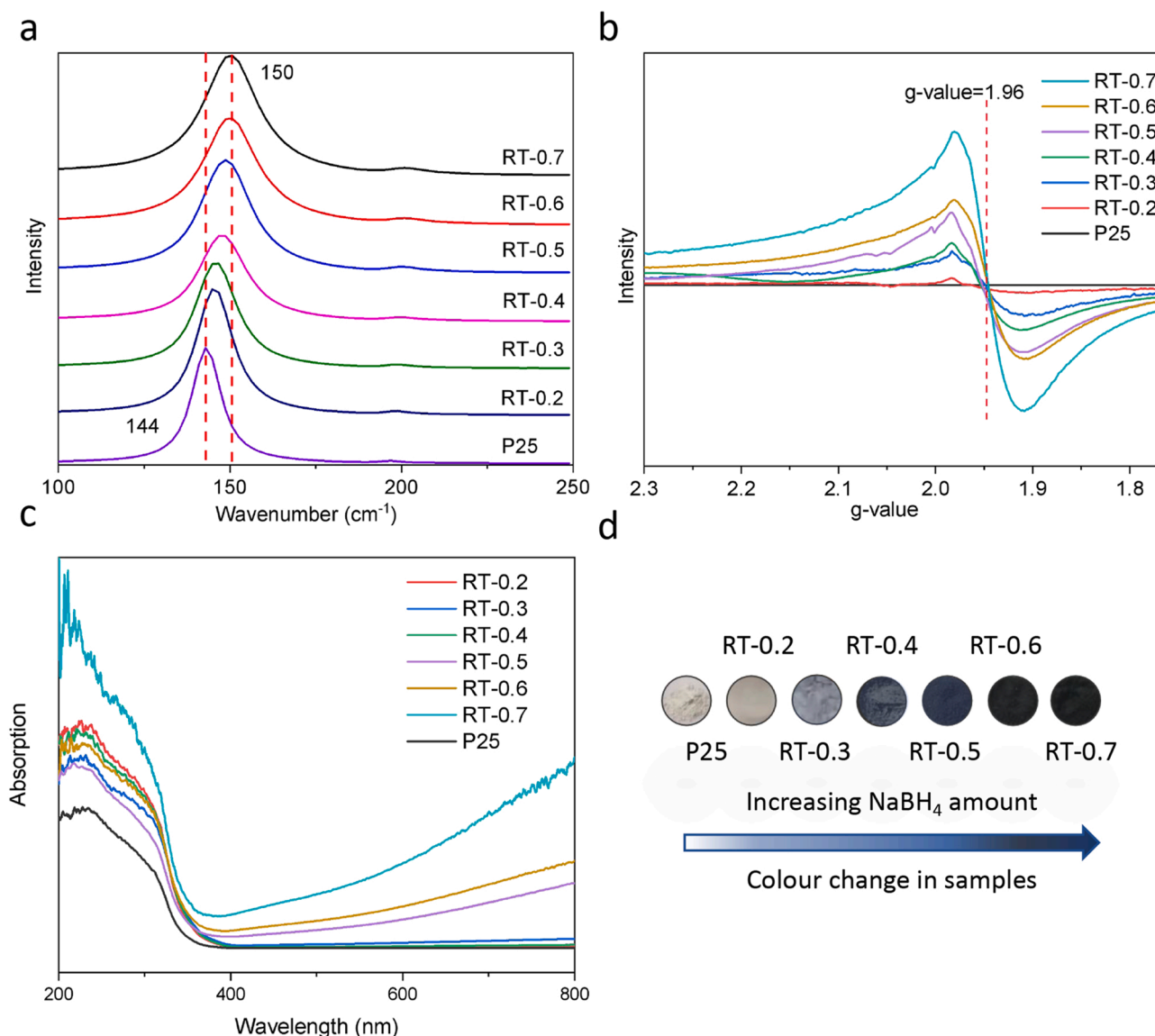
Fig. 2. (a) Raman spectra at 100–250 cm^{-1} (full Raman spectra are shown in Fig. S4), (b) EPR spectra recorded at 120 K (c) UV–vis diffuse reflectance spectra of P25 and all defected TiO$_2$. (d) Physical colour changes of P25 upon NaBH$_4$ chemical reduction.

forming a reducing environment for defect formation on TiO$_2$. As observed in Fig. 2a, with an increasing amount of NaBH$_4$ used, there is an evident shift towards higher wavenumber, from ~144 cm^{-1} in P25 to ~150 cm^{-1} in RT-0.7. As the Eg mode originates from symmetric stretching of the O-Ti-O bond, the presence of O$_v$ within the TiO$_2$ crystal will affect the Eg mode frequency [33,34]. When oxygen atoms are removed from the TiO$_2$ crystal, the Ti atoms will move closer to the other adjacent oxygen atoms, thus strengthen the remaining O-Ti-O bonds. Therefore, the observed blue shift in the Eg mode for the defected TiO$_2$ samples indicates there is an increase in the amount of O$_v$ within the TiO$_2$ crystal, due to the stronger O-Ti-O bonds.

Low temperature EPR analysis was performed to further verify O$_v$ formation for all the defected TiO$_2$ samples. As shown in Fig. 2b, signals at a g-value of ~1.96 is observed for all defected TiO$_2$ samples. The peak is attributed to the formation of Ti^{3+} sites upon chemical reduction [21, 30]. Removing one oxygen atom (representing the formation of one O$_v$) leaves two residual electrons that will subsequently be transferred to adjacent Ti^{4+} to form Ti^{3+} (Scheme S2). Therefore, the increasing EPR signal at the g-value of ~1.96 represents the increasing concentration of Ti^{3+} sites in the defected TiO$_2$ samples. The results also demonstrate that the higher the amount of NaBH$_4$ used during calcination, the higher the

concentration of Ti^{3+} and O$_v$ formed within the bulk crystal structure, which is consistent with the Raman results.

An observed change in optical properties of the TiO$_2$ also verifies the presence of O$_v$ in the defected TiO$_2$ samples. As demonstrated in the UV–vis absorption spectra (Fig. 2c), all defected TiO$_2$ samples exhibit enhanced visible light absorption in the range of 400–800 nm, corresponding to the colour change from white (bare P25) to dark blue or black (depending on the amount of O$_v$ formed). The absorption band edges of the defected P25 TiO$_2$ are also red shifted, signifying a narrower bandgap when compared to P25 (Fig. S5), due to the presence of defect states. This is supported by the same phenomenon observed in other studies which have reported on a narrowing of the bandgap for Ti^{3+}-containing TiO$_2$ samples [29,30].

3.2. Defect Induced Activity Enhancement

Photoluminescence (PL) occurs when electrons in the conduction band recombine with holes in the valence band. Consequently, PL spectra are commonly used to qualitatively compare the rate of charge recombination for different photocatalysts [3,30,35]. Although some studies use PL spectra as evidence to support the generated defect states,

the PL signals do not always decrease proportionally with increasing defect concentrations. This is because a continuous increase in defect states does not necessarily provide a corresponding decrease in charge recombination throughout the photocatalyst. As shown in Fig.S6 a-b, RT-0.7 displays a higher emission signal compared with RT-0.5. The higher emission signal derives from excessive bulk defects in RT-0.7 which act as recombination centers for the charge carriers. The higher recombination center concentration in RT-0.7 invokes a higher charge recombination rate which results in a higher PL emission when compared to RT-0.5. The phenomenon was also observed by Chen et al. when they introduced oxygen vacancies into a TiO2 matrix under a H2 atmosphere at elevated temperature [36]. The increase in reduction temperature induced a high concentration of surface oxygen defects which helped suppress charge recombination, subsequently lowering the PL emission signal. However, when the reduction temperature was increased to beyond 500 °C, an excessive number of defects formed with these now acting as charge carrier recombination sites resulting in a higher PL emission. In Fig. S6c and S6d, the broad and intensive emission in the 410–450 nm range is attributed to recombination of the photo-generated electrons and holes in the mixed phase TiO2 crystallite. Multiple PL signals in the visible region (430–550 nm) are apparent for all samples, which correspond to shallow traps on the surface and bulk defect sites. A detailed discussion on the PL spectra obtained from Raman and fluorescence spectrometry is included in Note. S2.

The results from the photoreforming of a 10 % ethanol solution for 6 h by the bare and defected TiO2 samples are shown in Fig. 3a. It is apparent from the result that an increased H2 evolution rate was observed for all the defected TiO2 samples. Increasing the amount of NaBH4 used to treat the samples sees the amount of H2 evolved also increase up to RT-0.5. Beyond RT-0.5, the H2 evolution rate decreases with increasing NaBH4 used, reflecting an increase in the O$_v$ concentration within the TiO2 samples (RT-0.6 and RT-0.7). The amounts of acetaldehyde and acetic acid generated over different samples are also shown in Fig. 3a, with a similar trend to the H2 evolution being displayed. With the increasing amount of NaBH4 used, organic production during the 6 h reaction timeframe increased from 0.14 mmol over P25 to 0.47 mmol over RT-0.5, after which it decreased to 0.23 mmol over RT-0.7. A detailed compilation of the products can be found in Table S4.

To further understand the variation in photoactivity with NaBH4 treatment, PEC measurements were performed to determine the difference in photocurrent density between the samples. Photocurrent density can indirectly indicate the relative amounts of active charges being generated and consumed within the system. During the measurements, a 30 s light pulse was employed as the excitation source. As shown in Fig. 3b, under the dark condition, a low current density (~1 uA cm^{-2}) was generated for all TiO2 samples at 0.22 V vs. Ag/AgCl. Upon irradiation, sample RT-0.5 exhibited a photocurrent density of up to 40 uA cm^{-2}, which is almost 10 times greater than that of bare P25 (~4 uA cm^{-2}). The observation mirrors the highest photoactivity exhibited by RT-0.5 during the ethanol photoreforming reaction, indicating the optimized charge carrier transfer and consumption by RT-0.5. The relationship between activity and defect will be further discussed later.

The HER performance of the defected TiO2 photocatalyst in this work is comparable to existing studies, as shown in Table. S5. Additional experiments were conducted using a 300 W Xe lamp as the light source in a top illumination system to provide a better comparison with other reports (Scheme S1b). The results are listed in Table. S5. A lower activity was delivered with the 300 W Xe lamp top illumination system, which is attributed to: (i) the lower portion of UV light in the Xe lamp's light spectrum; and (ii) the substantially larger irradiation area of spiral reactor when compared to the top illumination system (Scheme S1b). Further, 0.5 wt % Pt was loaded onto both P25 and RT-0.5 using an in-situ photo-deposition process to provide a performance comparison with other metal loaded catalysts. Note that most of the existing reports on alcohol photoreforming focused solely on the activity enhancement for hydrogen evolution, while selectivity was not investigated to any significant extent. In contrast, a detailed investigation on the quantity of gas and liquid phase products was completed in this work.

3.3. Selectivity indicated by H2 purity and liquid to gas phase carbon ratio

To understand the origin of product selectivity in the gas and liquid phases arising from the defected TiO2, consideration of the reaction pathway is needed. Based on the reaction pathways reported and the gas and liquid phase products identified in our work, the potential reaction pathway is proposed in Fig. 4a [18]. The observation of the 1-hydroxyethyl radical confirms that the first step of ethanol photoreforming on defected TiO2 involves C-H activation rather than O-H activation, whereby an α-H is abstracted from the ethanol molecule, as illustrated in Fig. 4a and Fig. S7 [37]. The 1-hydroxyethyl radical then undergoes additional h+ attack to form the desired product, acetaldehyde. Oxidation of acetaldehyde leads to the formation of acetic acid. The acetic acid may then be further oxidized into CO, CO2 and CH4 via a carbonyl route [38–41] or a CO route [38,42,43]. As mentioned earlier
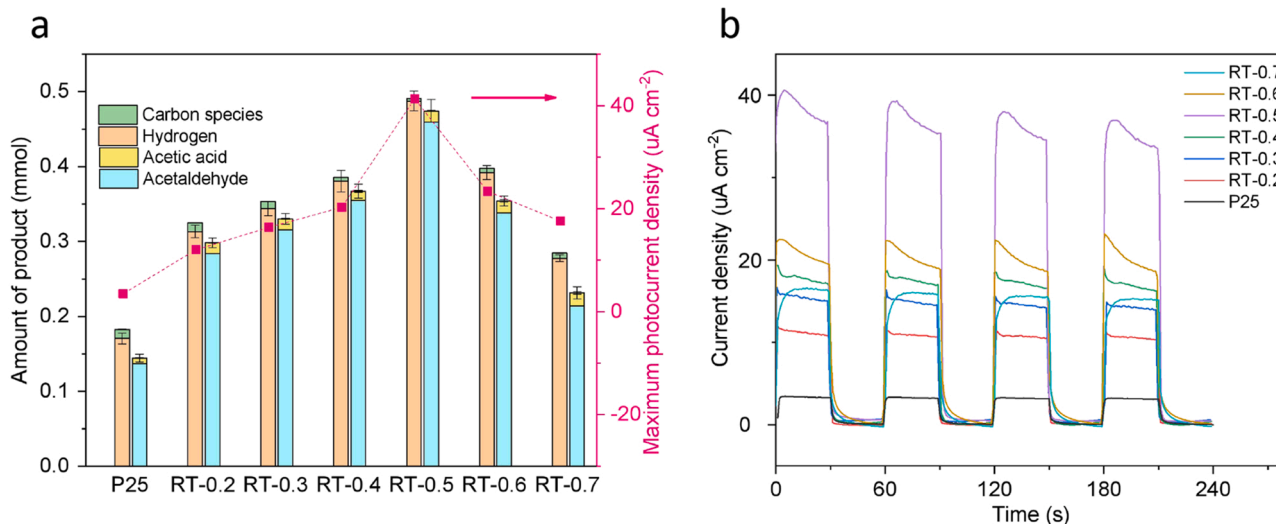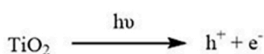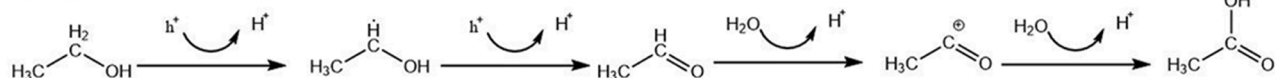

Fig. 3. (a) Gaseous and liquid products generated during 6 h of photoreforming of a 10 % ethanol solution by the bare and defected TiO2 samples. The activity of samples is in agreement with their maximum photocurrent density. (b) Transient photocurrent responses of the bare and defected TiO2 samples under an applied potential of 0 V vs. RHE in 0.2 M Na2SO4.
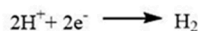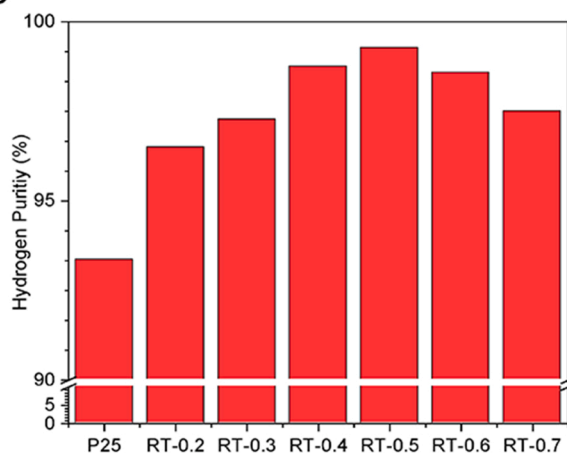
a

Charge carrier generation

$$TiO_2 \xrightarrow{h\upsilon} h^+ + e^-$$

Oxidation reaction

Reduction reaction
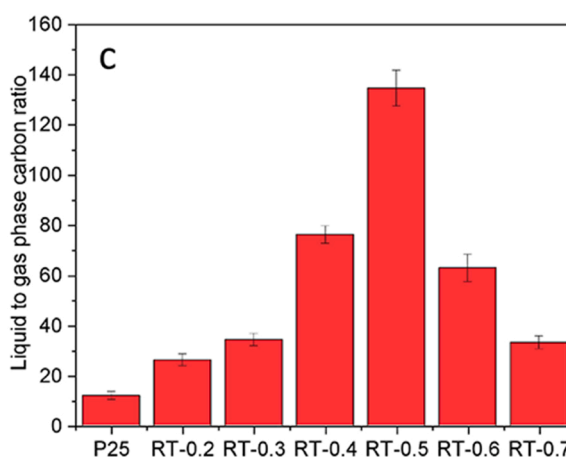
$$2H^+ + 2e^- \longrightarrow H_2$$

b

c

Fig. 4. (a) Proposed reaction pathway for the ethanol photoreforming reaction over bare and defected TiO_2 photocatalyst. (b) H_2 purity and (c) liquid to gas phase carbon ratio exhibited by the bare and defected TiO_2 catalysts.

on, it is desirable for the oxidation reaction to cease after acetaldehyde or acetic acid formation, rather than further oxidation to carbon-containing gaseous products.

In this study, we designated two important parameters to define the overall selectivity of the ethanol photoreforming reaction: (i) H_2 purity which is calculated based on the amount of H_2 generated versus the total amount of gas products, including CO, CO_2 and CH_4 (Eq. S1); (ii) liquid to gas phase carbon ratio (Eq. S2) which describes the carbon utilization efficiency and overall carbon product selectivity. The detailed rationalization of above two selectivity indicators were discussed in Note. S3. In an ideal photoreforming reaction, the H_2 purity should be close to 100 % (to eliminate the need for post-reaction gas separation) while simultaneously delivering a high liquid to gas phase carbon ratio. The complete degradation of ethanol into CO_2, as described by Eq. S3, provides 75 % H_2 purity with a zero liquid to gas phase carbon ratio (i.e., all the carbon species are oxidized into CO_2 and released into the gas phase).

As shown in Fig. 4b, the H_2 purity for bare P25 TiO_2 was 93.4 %, while sample RT-0.5 achieved a H_2 purity greater than 99 %. The increased purity is significant as a higher H_2 purity will decrease the load of the subsequent purification process. The results indicate that with a proper degree of defect engineering via chemical reduction, the purity of the generated H_2 can be improved. A similar trend was revealed for the liquid to gas phase carbon selectivity over the different samples. As shown in Fig. 4c, the liquid to gas phase carbon ratio over P25 was 11.9, which means one carbon atom was over-oxidized into gas products for every 13 carbon atoms participating in the oxidation reaction. In contrast, for the RT-0.5 sample, one carbon atom was over-

oxidized to a gas product while 134 carbon atoms were retained as liquid product. The above results clearly reveal an improved selectivity for defected TiO_2 when compared to P25, demonstrating capacity for the practical application to H_2 fuel cells and biomass utilization.

3.4. Stability in terms of activity and selectivity

To assess catalyst stability, a 24 h continuous reaction was conducted using 20 mg RT-0.5. The decrease in catalyst loading (compared to other photocatalytic tests) was to prevent over-pressurizing the closed reaction system. As shown in Fig. 5a-b, HER performance and the hydrogen purity remained stable over the 24 h, indicating a great stability in both activity and selectivity over defected TiO_2.

As for the selectivity aspect, the most selective catalyst, RT-0.5, was tested to ensure its stability. In this test, 80 mg catalysts and 100 ml 10 v/v % ethanol solution were used for 6 h as the first cycle. After reaction, liquid sample was collected and quantified. Solid particles were collected on a filter membrane and dispersed in a new batch of 100 ml 10 v/v % ethanol solution. The stability test contains for 4 cycles, and the results in selectivity were displayed in Fig. 5c-d. It is obvious that during the liquid sample taking and the particle recovery, a small portion of the catalyst will be lost, which may be responsible for the slight decrease in activity (Fig. 5c). However, the hydrogen purity and L/G carbon ratio remained similar throughout the four cycles of reaction, indicating stable selectivity throughout the reaction (Fig. 5d).
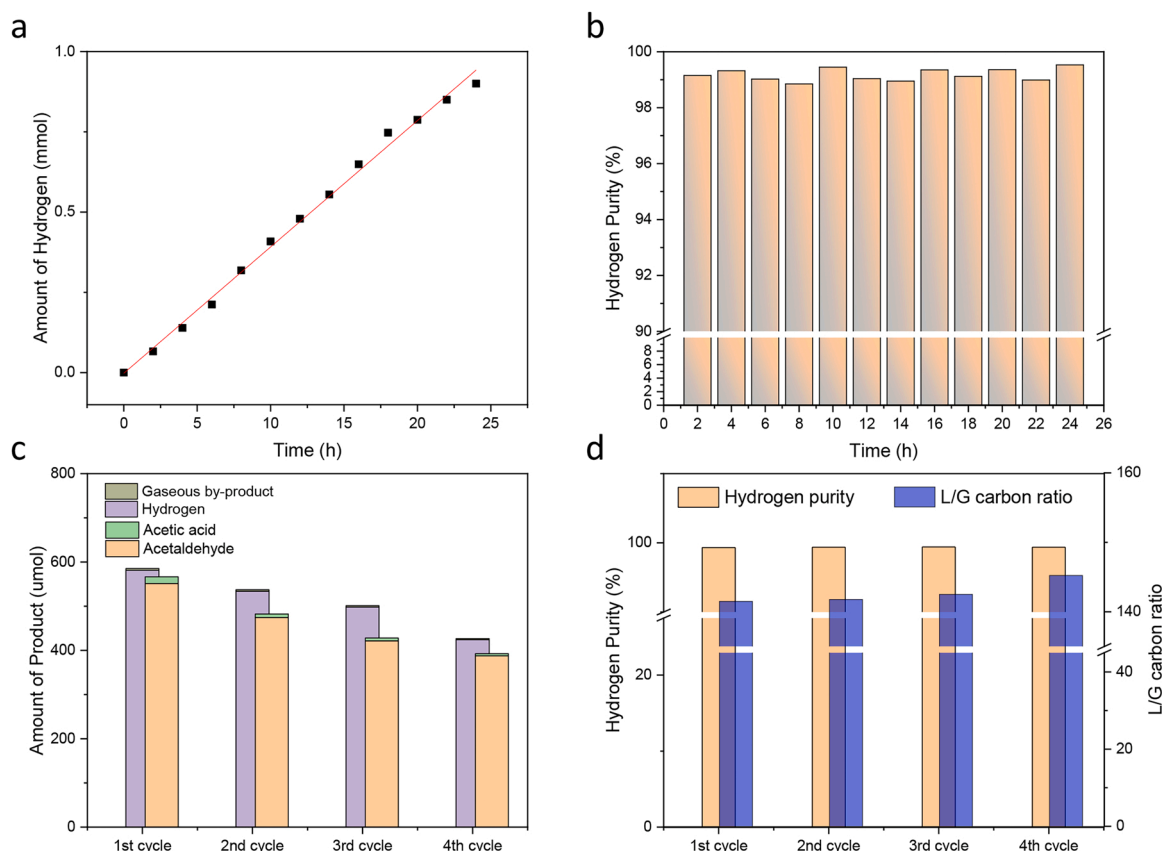
Fig. 5. Stability of RT-0.5 over 24 h of reaction in a 10 v/v % ethanol solution. (a) Hydrogen evolution reaction. (b) Hydrogen purity. Stability of RT-0.5 over 4 cycle of 4 h reaction in a 10 v/v % ethanol solution. (c) Amount of products in gas and liquid phase. (d) Hydrogen purity and liquid to gas phase carbon selectivity.

3.5. Surface Defect Regulated Selectivity

To establish the property-selectivity relationship, mechanistic studies are crucial in identifying the active species participating in the reaction. Under an anaerobic condition, the oxidation reaction is promoted by either direct photogenerated hole transfer or indirect radical reaction with hydroxyl radicals (OH•) and/or hydrogen peroxide (H_2O_2) [35,44]. To determine the potentially dominant pathway, active species trapping experiments were conducted. For OH• detection, dimethyl sulfoxide (DMSO), coumarin were determined to be the trapping agents, while $KMnO_4$ would be employed as trapping agents for H_2O_2. One molecule of DMSO can be oxidized into methanesulfonate by two hydroxyl radicals (Fig. S8). Consequently, the recovery rate of DMSO is inversely proportional to the amount of OH• radicals present in the system [45–47]. A high recovery rate (> 99 %) of DMSO was achieved for RT-0.5 upon 3 h UV illumination, suggesting the absence of OH• radicals during reaction (Table S6). This is further supported by the coumarin test, in which coumarin reacts with OH• to form 7-hydroxycoumarin (Fig. S9a) [48,49]. As demonstrated in Fig. S9b, one peak originating from coumarin is present, while no peak was observed for 7-hydroxycoumarin (at 456 nm) after the photoreforming reaction. Both the DMSO and coumarin experiments strongly affirm that OH• is not generated in the system. Similarly, the high recovery of $KMnO_4$ from the H_2O_2 trapping experiment verified the absence of H_2O_2 in the system (Fig. S10 and Note S1) [50]. Given OH• and H_2O_2 did not appear to contribute to the photoreforming process, direct oxidation by photo-generated holes on the surface of the defected TiO_2 is believed to be the dominant reaction pathway. Consequently, we can conclude that the ethanol oxidation was induced by direct hole transfer from the TiO_2. Taken from the outcome of the active species trapping experiments, ethanol needs to be adsorbed on the photocatalyst surface to initiate the

-OH activation reaction and oxidise ethanol into acetaldehyde via direct hole transfer. If acetaldehyde continues to be strongly absorbed on the surface after the initial activation, undesirable over-oxidation towards carbon-containing gas phase products will occur. Hole formation can occur on both rutile and anatase phases. However, the predominant crystal phase in P25 TiO_2 is anatase phase, while the rutile phase accounts for approximately 25 %. This suggests that the amount of exposed active sites available for surface reaction on rutile is comparatively lower than on anatase. In addition, it should be noted that the valence band position of rutile is similar to or slightly higher than that of anatase, which may also promote hole transfer from the rutile to anatase within the heterojunction structure [51]. Subsequently, DFT modelling was conducted to examine the difference in acetaldehyde chemisorption on defect-free and defected anatase surfaces. As shown in Fig. 6a, the adsorption of an acetaldehyde molecule is hindered by a pre-absorbed OH group on the O_v site on a defected TiO_2 surface. In contrast, the oxygen atom from the -CHO group will interact with the Ti atom on a defect-free TiO_2 surface, resulting in stronger adsorption (Fig. S11a). As a consequence, the adsorption energy of acetaldehyde on a defected surface (−0.65 eV) is lower than that of a defect-free surface (−0.76 eV). In other words, the chemisorption of acetaldehyde on a defected surface is weaker than that on a defect-free surface. The acetaldehyde intermediate will be more likely to be released from a defected TiO_2 surface instead of undergoing further oxidation, therefore, increasing the selectivity towards this compound. The adsorption configurations of ethanol on defect-free and defected anatase models were examined by DFT (as depicted in Fig. S11b and S11c). The results show that ethanol does not chemisorb onto either substrate, instead binding weakly through H-bonding interactions, with an adsorption energy of around −0.2 eV. Consequently, it is expected that there will be little difference in ethanol binding between the pristine and defected TiO_2.
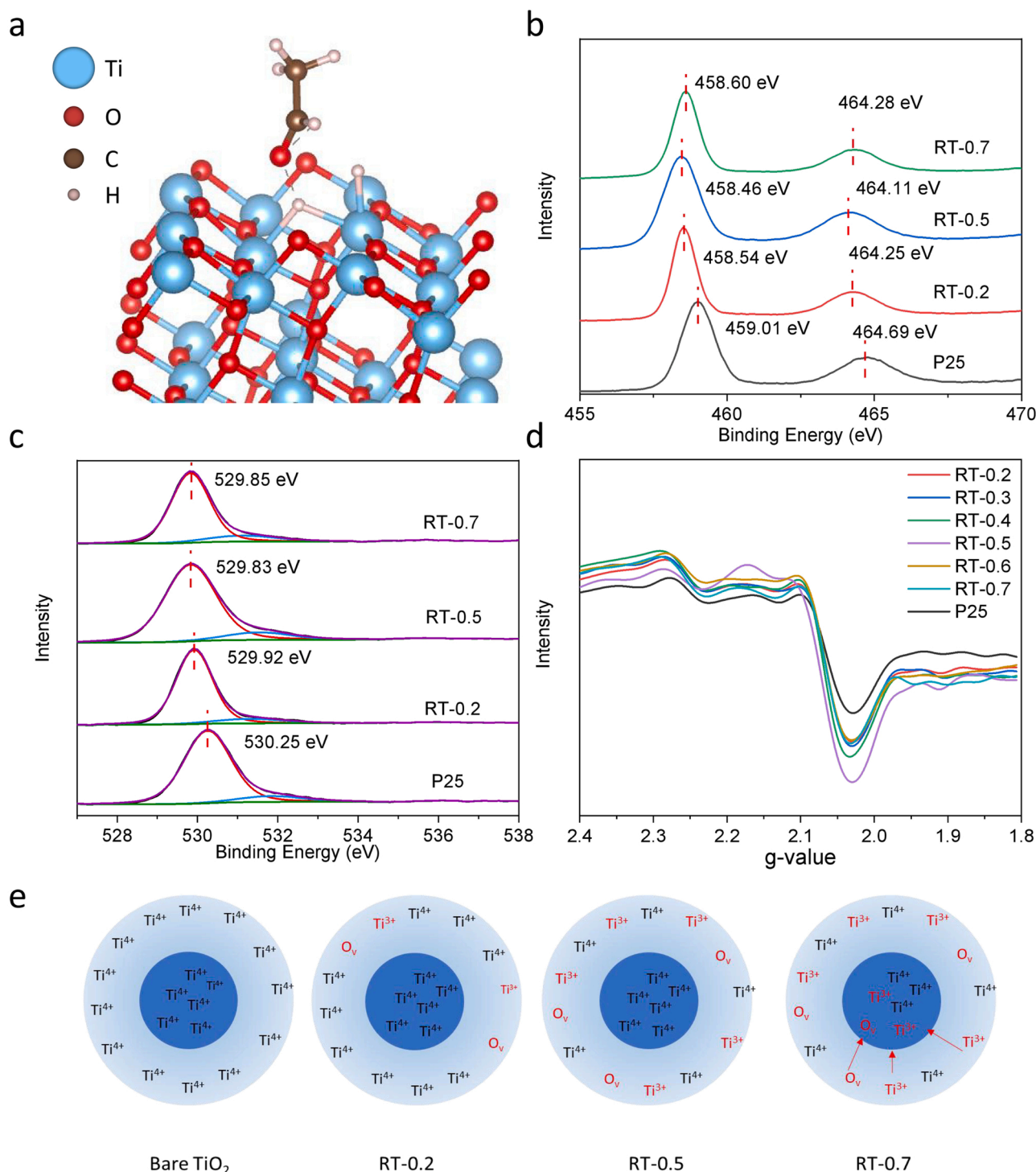
Fig. 6. (a) DFT model depicting the chemisorption of acetaldehyde on a defected TiO_2 surface, which contains an -OH group attached at the oxygen vacancy site. The Ti, O, C and H atoms are represented by blue, red, brown and pinkish-white spheres, respectively. High resolution XPS spectra of (b) Ti 2p and (c) O 1s orbits over bare TiO_2 and selected defected TiO_2 samples. (d) EPR spectra of defected and bare TiO_2 samples recorded at room temperature (293 K). (e) schematic of defect generation and subsequent migration in TiO_2 exposed to increasing amounts of $NaBH_4$ reductant.

To further understand the factors affecting selectivity during the ethanol photoreforming reaction, room temperature EPR and XPS were employed. Bulk characterization methods, such as Raman (Fig. 2a) and low temperature EPR (Fig. 2b), revealed that using higher $NaBH_4$ amounts led to greater O_v formation within the bulk TiO_2 crystal. However, optimum selectivity was exhibited by RT-0.5 as opposed to RT-0.7 which contained the highest amount of O_v. As shown by the active species trapping findings, the reaction was dominated by surface

chemisorption. Hence, employing a characterization method which targets the surface properties of the TiO_2 (i.e., XPS) has is advantageous for investigating surface defects [52]. As shown in Fig. S12, the XPS survey scan demonstrates the presence of Ti and O. High resolution XPS of the O 1s spectral region is provided in Fig. 6b. After deconvolution, two peaks at ~530 eV and ~531 eV are apparent. The former peak is assigned to lattice oxygen in the TiO_2 matrix, while the latter peak is attributed to -OH groups on the surface. Comparing with bare TiO_2,

there is a clear peak shift towards a lower binding energy for all defected samples. A similar effect is present in the high resolution XPS spectra of Ti 2p, as shown in Fig. 6c. Peaks at 459.01 eV and 464.69 eV are detected for the bare TiO_2 sample, which is consistent with previous literature [30]. Following chemical reduction, the peaks shift towards a lower binding energy for all defected TiO_2 samples. As reported elsewhere, Ti atom removal from TiO_2 resulted in a peak shift towards higher binding energy for both the O 1s and Ti 2p peaks. In contrast, a peak shift to a lower binding energy occurred when oxygen atoms were removed [53]. Subsequently, the findings demonstrate that the $NaBH_4$ reductant can remove oxygen atom from the TiO_2 surface to create O_v.

As the binding energy in XPS represents charge densities of surface elements, a larger shift in binding energy reflects a bigger difference in electron density of the surface element. It is worth noting that the RT-0.5 XPS spectra for Ti 2p and O 1s exhibited a larger negative shift than RT-0.7 (Fig. 6b-c). With higher $NaBH_4$ dosage, the difference in peak shift is smaller when comparing RT-0.5 and RT-0.7, suggesting there is a decreased O_v concentration on the RT-0.7 surface. With continual removal of oxygen from the TiO_2 surface and the subsequent formation of Ti^{3+} sites, the surface will become increasingly negatively charged leading to negative shift in the binding energies for Ti 2p and O 1s. Upon reaching a saturation point, the defects may then begin to migrate into the bulk of the material, shifting the binding energy to more positive values (relative to RT-0.5). That is, when the O_v amount on the surface becomes saturated, oxygen tends to move from the bulk towards the surface, creating more oxygen vacancies in the bulk while the amount of surface O_v stabilizes. This effect has also been reported by Yu et al. when anatase TiO_2 was calcined at various temperatures for different durations under a H_2 atmosphere to produce defects [29]. At longer reduction times, surface Ti^{3+} sites moved into bulk material and the surface was increasingly occupied by O^{2-} and O^-, which were generated by the interaction between oxygen and the surface defects. These oxygen radical species are visible in the room temperature EPR spectrum at a g-value of ~2.002 as seen in Fig. 6d. As the amount of $NaBH_4$ used increases, more surface defects are generated from P25 to RT-0.5, as demonstrated by the increasing peak intensity at g-value 2.002. However, beyond RT-0.5, the peak intensity is diminished, indicating a decrease in surface O_v for RT-0.6 and RT-0.7. The trend agrees with the earlier XPS results, further confirming the saturation and subsequent migration of surface defects into the bulk structure (Fig. 6e). As revealed by both low temperature and room temperature EPR, Raman spectroscopy and XPS, although the amount of O_v increased with the amount of $NaBH_4$ used during the reduction process, RT-0.5 displayed the highest concentration of surface O_v and delivered the best activity and selectivity of the samples examined. The concentration of oxygen vacancies was manipulated by adjusting the amount of $NaBH_4$ used during the chemical reduction process. It is also apparent that an increase in $NaBH_4$ concentration at low levels results in an increased in surface defects. Interestingly, beyond a certain threshold concentration (0.5 g $NaBH_4$ per 1 g P25 TiO_2 in this work), further increases in $NaBH_4$ result in a higher overall defect concentration at the expense of a reduction in surface defect concentration. This is due to the migration of surface oxygen vacancies into the bulk structure. It was reported that although defects contribute to the light absorption and colour shift from white to blue, there is no guarantee that the introduction of defects will enhance activity. For instance, it has been demonstrated that bulk defects increased at the expense of surface defects in hydrogen annealed-TiO_2. No significant and corresponding improvement in photoactivity was observed, as the lifetime of the photogenerated charge carriers was reduced by excessive bulk defects [54]. In our work, the oxygen vacancy concentration is regulated by adjusting the amount of $NaBH_4$ used during the chemical reduction process. The treatment generates surface defects which, in turn, boost TiO_2 photoactivity until a point is reached where bulk defects then begin to form in the TiO_2. As the chemisorption of -CHO groups on surface O_v influences the selectivity towards aldehydes, the defected TiO_2 should also offer better aldehyde selectivity for other alcohols, such as methanol and isopropanol. Additional experiments with methanol and isopropanol as reactant were conducted to verify this hypothesis. The corresponding reaction were conducted with similar condition as described in experimental section. Instead, 10 v/v % ethanol solution was replaced by 10 v/v % methanol solution and isopropanol solution, respectively. As observe in Fig. S13 & Table. S7, in gas phase product, P25 TiO_2 shown lower activity and selectivity comparing with RT-0.5. More importantly, RT-0.5 also exhibits a better selectivity than P25 TiO_2 when loaded with the Pt co-catalyst. The hydrogen purity and liquid to gas phase carbon ratio for Pt/RT-0.5 is higher than for Pt/P25 TiO_2, which can be attributed to the improved surface defect-regulated chemisorption. The enhanced activity should be ascribed to the improvement in light absorption and charge carrier separation. The better hydrogen purity should be attributed to the surface O_v induced chemisorption behavior.

4. Conclusion

In this work, defected TiO_2 was prepared using a facile $NaBH_4$ reduction method. As revealed by UV–vis DRS, PL and PEC analyses, defecting the TiO_2 invokes greater light absorption, a narrower bandgap and suppressed charge carrier recombination, which improves its photoreforming performance. For a 10 v/v % ethanol solution, the defected TiO_2 displayed higher activity and selectivity towards H_2 and value-added liquid products when compared to bare TiO_2. The best-performing sample was RT-0.5 which produced 0.48 mmol H_2 at high purity (greater than 99 %) along with 0.47 mmol of liquid acetaldehyde and acetic acid over a 6 h time frame. The volume of H_2 and liquid organic generated by RT-0.5 was ~3 time higher than bare TiO_2. The photooxidation reaction occurred on the surface of the TiO_2, as the active species were determined to be photogenerated holes. DFT calculations demonstrated that surface O_v weakened surface adsorption of the intermediate product (i.e., acetaldehyde) which regulated the reaction pathway to suppress over-oxidation. Increasing the $NaBH_4$ amount used during TiO_2 treatment increased the O_v site presence on the TiO_2 surface. A relationship between the O_v presence and photoreforming activity for the defected TiO_2 was observed, indicating the O_v behaved as active sites for the photoreforming reaction. Beyond an optimum $NaBH_4$ pretreatment amount (RT-0.5) the photoreforming activity decreased. This was attributed O_v saturation of the surface having been reached. At this point, excess O_v formed then began to migrate into the bulk structure and act as a recombination centre causing a negative effect on photoreforming activity. The optimum activity and selectivity exhibited by RT-0.5 is attributed to it having the highest concentration of surface O_v. The work demonstrates a facile means by which the photoreforming performance of simple TiO_2 can be elevated through simple surface defect engineering of the particles.

CRediT authorship contribution statement

Jiajun Zhang: Conceptualization, Methodology, Investigation, Validation, Data curation, Writing - original draft. **Cui Ying Toe:** Methodology, Supervision, Conceptualization, Data curation, Writing - review & editing. **Priyank Kumar:** Visualization, Methodology. **Jason Scott:** Conceptualization, Supervision, Funding acquisition, Writing - review & editing. **Rose Amal:** Conceptualization, Supervision, Funding acquisition, Writing - review & editing.

Declaration of Competing Interest

Data Availability

Data will be made available on request.

Acknowledgments

Appendix A. Supporting information

Supplementary data associated with this article can be found in the online version at doi:10.1016/j.apcatb.2023.122765.

References

[1] K.T. Møller, T.R. Jensen, E. Akiba, H.-w Li, Hydrogen-A sustainable energy carrier, Prog. Nat. Sci. Mater. Int. 27 (2017) 34–40.
[2] O. Faye, J. Szpunar, U. Eduok, A critical review on the current technologies for the generation, storage, and transportation of hydrogen, Int. J. Hydrogen Energy 47 (2022) 13771–13802.
[3] H. Song, S.Q. Luo, H.M. Huang, B.W. Deng, J.H. Ye, Solar-driven hydrogen production: recent advances, challenges, and future perspectives, Acs Energy Lett. 7 (2022) 1043–1065.
[4] N. Fajrina, M. Tahir, A critical review in strategies to improve photocatalytic water splitting towards hydrogen production, Int. J. Hydrogen Energy 44 (2019) 540–577.
[5] A.A. Ismail, D.W. Bahnemann, Photochemical splitting of water for hydrogen production by photocatalysis: a review, Sol. Energ. Mater. Sol. C 128 (2014) 85–101.
[6] R. Sirohi, A. Kumar Pandey, P. Ranganathan, S. Singh, A. Udayan, M. Kumar Awasthi, A.T. Hoang, C.R. Chilakamarry, S.H. Kim, S.J. Sim, Design and applications of photobioreactors- a review, Bioresour. Technol. 349 (2022), 126858.
[7] G. Lopez, L. Santamaria, A. Lemonidou, S. Zhang, C. Wu, A.T. Sipra, N. Gao, Hydrogen generation from biomass by pyrolysis, Nat. Rev. Methods Prim. 2 (2022) 1–13.
[8] M.I. Taipabu, K. Viswanathan, W. Wu, N. Hattu, A. Atabani, A critical review of the hydrogen production biomass-based feedstocks: challenge, solution, and future prospect, Process Saf. Environ. Prot. 164 (2022) 384–407.
[9] T. Lepage, M. Kammoun, Q. Schmetz, A. Richel, Biomass-to-hydrogen: a review of main routes production, processes evaluation and techno-economical assessment, Biomass Bioenerg. 144 (2021), 105920.
[10] H. Luo, J. Barrio, N. Sunny, A. Li, L. Steier, N.I. Shah, I.E.L. Stephens, M.M. Titirici, Progress and perspectives in photo- and electrochemical-oxidation of biomass for sustainable chemicals and hydrogen production, Adv. Energy Mater. 11 (2021) 2101180.
[11] D.B. Pal, A. Singh, A. Bhatnagar, A review on biomass based hydrogen production technologies, Int. J. Hydrogen Energy 43 (2021) 1461–1480.
[12] C. Li, J. Liu, H. Li, K. Wu, J. Wang, Q. Yang, Covalent organic frameworks with high quantum efficiency in sacrificial photocatalytic hydrogen evolution, Nat. Commun. 13 (2022) 2357.
[13] J. Ran, G. Gao, F.-T. Li, T.-Y. Ma, A. Du, S.-Z. Qiao, Ti3C2 MXene co-catalyst on metal sulfide photo-absorbers for enhanced visible-light photocatalytic hydrogen production, Nat. Commun. 8 (2017) 13907.
[14] M. Balat, H. Balat, C. Oz, Progress in bioethanol processing, Prog. Energ. Combust. 34 (2008) 551–573.
[15] B. Hahn-Hägerdal, M. Galbe, M.-F. Gorwa-Grauslund, G. Lidén, G. Zacchi, Bio-ethanol—the fuel of tomorrow from the residues of today, Trends Biotechnol. 24 (2006) 549–556.
[16] S. Rajeswari, D. Baskaran, P. Saravanan, M. Rajasimman, N. Rajamohan, Y. Vasseghian, Production of ethanol from biomass—Recent research, scientometric review and future perspectives, Fuel 317 (2022), 123448.
[17] Z.H.N. Al-Azri, W.-T. Chen, A. Chan, V. Jovic, T. Ina, H. Idriss, G.I.N. Waterhouse, The roles of metal co-catalysts and reaction media in photocatalytic hydrogen production: performance evaluation of M/TiO2 photocatalysts (M = Pd, Pt, Au) in different alcohol–water mixtures, J. Catal. 329 (2015) 355–367.
[18] A.V. Puga, Photocatalytic production of hydrogen from biomass-derived feedstocks, Coord. Chem. Rev. 315 (2016) 1–66.
[19] S. Chakraborty, V. Aggarwal, D. Mukherjee, K. Andras, Biomass to biofuel: a review on production technology, Asia-Pac. J. Chem. Eng. 7 (2012) 254–262.
[20] M. Van der Stelt, H. Gerhauser, J. Kiel, K. Ptasinski, Biomass upgrading by torrefaction for the production of biofuels: a review, Biomass Bioenerg. 35 (2011) 3748–3762.
[21] X. Chen, L. Liu, P.Y. Yu, S.S. Mao, Increasing solar absorption for photocatalysis with black hydrogenated titanium dioxide nanocrystals, Science 331 (2011) 746–750.
[22] Y. Nosaka, A. Nosaka, Understanding hydroxyl radical ((OH)-O-center dot) generation processes in photocatalysis, Acs Energy Lett. 1 (2016) 356–359.
[23] X. Zhang, L. Luo, R.P. Yun, M. Pu, B. Zhang, X. Xiang, Increasing the activity and selectivity of TiO2-supported Au catalysts for renewable hydrogen generation from ethanol photoreforming by engineering Ti3+ defects, Acs Sustain. Chem. Eng. 7 (2019) 13856–13864.
[24] Y.T. Cui, C. Tsounis, J. Zhang, H. Masood, D. Gunawan, J. Scott, R. Amal, Advancing photoreforming of organics: highlights on photocatalyst and system designs for selective oxidation reactions, Energy Environ. Sci. 14 (2021) 1140–1175.
[25] W. Fang, M. Xing, J. Zhang, A new approach to prepare Ti3+ self-doped TiO2 via NaBH4 reduction and hydrochloric acid treatment, Appl. Catal. B: Environ. 160–161 (2014) 240–246.
[26] D. Ariyanti, L. Mills, J. Dong, Y. Yao, W. Gao, NaBH4 modified TiO2: Defect site enhancement related to its photocatalytic activity, Mater. Chem. Phys. 199 (2017) 571–576.
[27] H. Chen, J. Liang, L. Li, B. Zheng, Z. Feng, Z. Xu, Y. Luo, Q. Liu, X. Shi, Y. Liu, S. Gao, A.M. Asiri, Y. Wang, Q. Kong, X. Sun, Ti2O3 nanoparticles with Ti(3+) sites toward efficient NH3 electrosynthesis under ambient conditions, ACS Appl. Mater. Interfaces 13 (2021) 41715–41722.
[28] Y. Yu, Y. Zhao, Y.L. Qiao, Y. Feng, W.L. Li, W.D. Fei, Defect engineering of rutile TiO2 ceramics: Route to high voltage stability of colossal permittivity, J. Mater. Sci. Technol. 84 (2021) 10–15.
[29] X. Yu, B. Kim, Y.K. Kim, Highly enhanced photoactivity of anatase TiO2 nanocrystals by controlled hydrogenation-induced surface defects, Acs Catal. 3 (2013) 2479–2486.
[30] A. Naldoni, M. Altomare, G. Zoppellaro, N. Liu, S. Kment, R. Zboril, P. Schmuki, Photocatalysis with reduced TiO2: from black TiO2 to cocatalyst-free hydrogen production, Acs Catal. 9 (2019) 345–364.
[31] J.J. Cai, M.H. Zhou, Y.W. Pan, X.D. Du, X.Y. Lu, Extremely efficient electrochemical degradation of organic pollutants with co-generation of hydroxyl and sulfate radicals on Blue-TiO2 nanotubes anode, Appl. Catal. B-Environ. 257 (2019), 117902.
[32] X. Wang, W. Shi, S. Wang, H. Zhao, J. Lin, Z. Yang, M. Chen, L. Guo, Two-dimensional amorphous TiO2 nanosheets enabling high-efficiency photoinduced charge transfer for excellent SERS activity, J. Am. Chem. Soc. 141 (2019) 5856–5862.
[33] T. Gakhar, A. Hazra, Oxygen vacancy modulation of titania nanotubes by cathodic polarization and chemical reduction routes for efficient detection of volatile organic compounds, Nanoscale 12 (2020) 9082–9093.
[34] H. Xie, N. Li, X.Z. Chen, J.Z. Jiang, X.J. Zhao, Surface oxygen vacancies promoted photodegradation of benzene on TiO2 film, Appl. Surf. Sci. 511 (2020), 145597.
[35] O. Al-Madanat, Y. Alsalka, M. Curti, R. Dillert, D.W. Bahnemann, Mechanistic insights into hydrogen evolution by photocatalytic reforming of naphthalene, Acs Catal. 10 (2020) 7398–7412.
[36] X. Chen, L. Liu, P.Y. Yu, S.S. Mao, Increasing solar absorption for photocatalysis with black hydrogenated titanium dioxide nanocrystals, Science 331 (2011) 746–750.
[37] F. Peyrot, S. Lajnef, D.-L. Versace, Electron paramagnetic resonance spin trapping (EPR–ST) technique in photopolymerization processes, Catalysts 12 (2022) 772.
[38] M. Bowker, Photocatalytic hydrogen production and oxygenate photoreforming, Catal. Lett. 142 (2012) 923–929.
[39] X. Fu, X. Wang, D.Y.C. Leung, Q. Gu, S. Chen, H. Huang, Photocatalytic reforming of C3-polyols for H2 production, Appl. Catal. B: Environ. 106 (2011) 681–688.
[40] Q. Gu, X. Fu, X. Wang, S. Chen, D.Y.C. Leung, X. Xie, Photocatalytic reforming of C3-polyols for H2 production, Appl. Catal. B: Environ. 106 (2011) 689–696.
[41] G. Han, Y.H. Jin, R.A. Burgess, N.E. Dickenson, X.M. Cao, Y. Sun, Visible-light-driven valorization of biomass intermediates integrated with H2 production catalyzed by ultrathin Ni/CdS nanosheets, J. Am. Chem. Soc. 139 (2017) 15584–15587.
[42] H. Bahruji, M. Bowker, P.R. Davies, L.S. Al-Mazroai, A. Dickinson, J. Greaves, D. James, L. Millard, F. Pedrono, Sustainable H2 gas production by photocatalysis, J. Photochem. Photobiol. A: Chem. 216 (2010) 115–118.
[43] M. Bowker, Sustainable hydrogen production by the application of ambient temperature photocatalysis, Green Chem. 13 (2011) 2235–2246.
[44] J. Xu, N. Sahai, C.M. Eggleston, M.A.A. Schoonen, Reactive oxygen species at the oxide/water interface: formation mechanisms and implications for prebiotic chemistry and the origin of life, Earth Planet Sc. Lett. 363 (2013) 156–167.
[45] A. Pielesz, A. Gawlowski, D. Binias, R. Bobinski, M. Kawecki, A. Klama-Baryla, D. Kitala, W. Labus, J. Glik, J. Paluch, The role of dimethyl sulfoxide (DMSO) in ex-vivo examination of human skin burn injury treatment, Spectrochim. Acta A Mol. Biomol. Spectrosc. 196 (2018) 344–352.
[46] E.M. Rodríguez, U.J. von Gunten, Generation of hydroxyl radical during chlorination of hydroxyphenols and natural organic matter extracts, Water Res. 177 (2020), 115691.
[47] G. Žerjav, A. Albreht, I. Vovk, A. Pintar, Revisiting terephthalic acid and coumarin as probes for photoluminescent determination of hydroxyl radical formation rate in heterogeneous photocatalysis, Appl. Catal. A: Gen. 598 (2020), 117566.
[48] H.Y. Gao, C.H. Huang, L. Mao, B. Shao, J. Shao, Z.Y. Yan, M. Tang, B.Z. Zhu, First direct and unequivocal electron spin resonance spin-trapping evidence for pH-

dependent production of hydroxyl radicals from sulfate radicals, Environ. Sci. Technol. 54 (2020) 14046–14056.

[49] V. Leandri, J.M. Gardner, M. Jonsson, Coumarin as a quantitative probe for hydroxyl radical formation in heterogeneous photocatalysis, J. Phys. Chem. C 123 (2019) 6667–6674.

[50] T.M. Gill, X. Zheng, Comparing methods for quantifying electrochemically accumulated H2O2, Chem. Mater. 32 (2020) 6285–6294.

[51] D.C. Hurum, A.G. Agrios, K.A. Gray, T. Rajh, M.C. Thurnauer, Explaining the enhanced photocatalytic activity of Degussa P25 mixed-phase TiO2 using EPR, J. Phys. Chem. B 107 (2003) 4545–4549.

[52] G. Greczynski, L. Hultman, X-ray photoelectron spectroscopy: towards reliable binding energy referencing, Prog. Mater. Sci. 107 (2020).

[53] S. Wang, L. Pan, J.J. Song, W. Mi, J.J. Zou, L. Wang, X. Zhang, Titanium-defected undoped anatase TiO2 with p-type conductivity, room-temperature ferromagnetism, and remarkable photocatalytic performance, J. Am. Chem. Soc. 137 (2015) 2975–2983.

[54] S.K. Cushing, F. Meng, J. Zhang, B. Ding, C.K. Chen, C.-J. Chen, R.-S. Liu, A. D. Bristow, J. Bright, P. Zheng, N. Wu, Effects of defects on photocatalytic activity of hydrogen-treated titanium oxide nanobelts, Acs Catal. 7 (2017) 1742–1748.